JGR Atmospheres

RESEARCH ARTICLE
10.1029/2021JD036232

Multi-Scale Kelvin-Helmholtz Instability Dynamics Observed by PMC Turbo on 12 July 2018: 1. Secondary Instabilities and Billow Interactions

C. Bjorn Kjellstrand[1,2], David C. Fritts[3], Amber D. Miller[1,4], Bifford P. Williams[3], Natalie Kaifler[5], Christopher Geach[6,7], Shaul Hanany[7], Bernd Kaifler[5], Glenn Jones[8], Michele Limon[9], Jason Reimuller[10], and Ling Wang[3]

[1]Department of Physics, Columbia University, New York, NY, USA, [2]School of Earth and Space Exploration, Arizona State University, Tempe, AZ, USA, [3]Boulder Division, GATS, Boulder, CO, USA, [4]Department of Physics and Astrometry, University of Southern California, Los Angeles, CA, USA, [5]German Aerospace Center (DLR), Munich, Germany, [6]German Aerospace Center (DLR), Neustrelitz, Germany, [7]School of Physics and Astronomy, University of Minnesota, Minneapolis, MN, USA, [8]Rigetti Computing, Berkeley, CA, USA, [9]Department of Physics and Astronomy, University of Pennsylvania, Philadelphia, PA, USA, [10]Integrated Spaceflight Services, Boulder, CO, USA

This article is a companion to Fritts et al. (2022), https://doi.org/10.1029/2021JD035834

Key Points:

- First observation of unambiguous secondary Kelvin-Helmholtz instabilities in high-resolution images of the polar mesospheric cloud layer
- Identification and quantification of Kelvin-Helmholtz billow interactions leading to tubes and knots and accelerated billow breakdown
- Estimation of turbulence Reynolds number $Re_{turb} \sim 5{,}000$ and $\nu_{turb} \sim 3$ times larger than the kinematic viscosity

Correspondence to:
C. B. Kjellstrand,
ckjellst@asu.edu

Citation:
Kjellstrand, C. B., Fritts, D. C., Miller, A. D., Williams, B. P., Kaifler, N., Geach, C., et al. (2022). Multi-scale Kelvin-Helmholtz instability dynamics observed by PMC Turbo on 12 July 2018: 1. Secondary instabilities and billow interactions. *Journal of Geophysical Research: Atmospheres*, *127*, e2021JD036232. https://doi.org/10.1029/2021JD036232

Received 22 NOV 2021
Accepted 19 JUL 2022

Abstract The Polar Mesospheric Cloud (PMC) Turbulence experiment performed optical imaging and Rayleigh lidar PMC profiling during a 6-day flight in July 2018. A mosaic of seven imagers provided sensitivity to spatial scales from ~20 m to 100 km at a ~2-s cadence. Lidar backscatter measurements provided PMC brightness profiles and enabled definition of vertical displacements of larger-scale gravity waves (GWs) and smaller-scale instabilities of various types. These measurements captured an interval of strong, widespread Kelvin-Helmholtz instabilities (KHI) occurring over northeastern Canada on July 12, 2018 during a period of significant GW activity. This paper addresses the evolution of the KHI field and the characteristics and roles of secondary instabilities within the KHI. Results include the imaging of secondary KHI in the middle atmosphere and multiple examples of KHI "tube and knot" (T&K) dynamics where two or more KH billows interact. Such dynamics have been identified clearly only once in the atmosphere previously. Results reveal that KHI T&K arise earlier and evolve more quickly than secondary instabilities of uniform KH billows. A companion paper by Fritts et al. (2022), https://doi.org/10.1029/2021JD035834 reveals that they also induce significantly larger energy dissipation rates than secondary instabilities of individual KH billows. The expected widespread occurrence of KHI T&K events may have important implications for enhanced turbulence and mixing influencing atmospheric structure and variability.

1. Introduction

Instabilities and turbulence occurring within the larger-scale motion field play fundamental roles in the circulation, structure, and variability of the atmosphere from the surface into the mesosphere and lower thermosphere (MLT). These dynamics arise in response to gravity waves (GWs) that contribute the major vertical transports of energy and momentum from a wide range of tropospheric sources to altitudes extending into the MLT (see Fritts & Alexander, 2003, for a review). GW amplitude increases with increasing altitude and decreasing density, and diverse superpositions of GWs and fine-structure fields enable a wide range of instabilities that contribute to turbulence and mixing throughout the atmosphere. One class of these dynamics, Kelvin-Helmholtz instabilities (KHI) that arise at unstable shear layers, has been the subject of observations in the atmosphere, oceans, and laboratory, and related theory and modeling, spanning ~60 years. More recent MLT observations reveal the widespread occurrence of large-scale KHI that may contribute significant turbulence and mixing in the MLT, but which have not been investigated, nor accounted for, in large-scale modeling of the MLT to date.

The earliest MLT study by Witt (1962) employed ground-based stereo Polar Mesospheric Cloud (PMC) imaging from northern Sweden in 1958 and described the GW and embedded KHI responses with remarkable accuracy and foresight. Other early observations in the atmosphere, ocean, and laboratory further quantified KHI scales, evolutions, and their dependence on the environmental Richardson number, *Ri*, and Reynolds number, *Re* (Browning & Watkins, 1970; Ludlam, 1967; Scorer, 1969; Scorer & Wilson, 1963; Thorpe, 1971, 1973a, 1973b; Woods, 1968; Woods & Wiley, 1972). Subsequent laboratory and early modeling and theoretical studies revealed instabilities driving KH billow breakdown, including (a) convective instabilities (CI) within the outer billows

where entrainment from below and above yield inverted density gradients, (b) secondary KHI in the stratified braids between and around intensifying billows, (c) pairing of adjacent billows for sufficiently low *Ri* and high *Re*, and (d) instabilities arising where adjacent KH billows are mis-aligned, discontinuous, or varying along their axes leading to transitional dynamics described by Thorpe as "tubes and knots" (T&K) (e.g., Fritts, 1984; Klaassen & Peltier, 1985, 1990; Patnaik et al., 1976; Thorpe, 1985, 1987). Laboratory examples and representations of these various KHI secondary instabilities were provided in Thorpe (1987).

More recently, Thorpe (2002) called attention to evidence for KHI T&K dynamics in thin cloud layers, but no direct imaging evidence for these dynamics in the MLT was discovered until the serendipitous high-resolution hydroxl (OH) airglow imaging over the Andes Lidar Observatory reported by Hecht et al. (2021). Insights from these observations suggest that previous OH airglow and PMC imaging of KHI dynamics also contained evidence for T&K dynamics, but these were not specifically identified in those studies (e.g., Baumgarten & Fritts, 2014; Fritts, Baumgarten, et al., 2014; Hecht et al., 2014). Recent imaging radar observations described by Chau et al. (2020) also showed evidence of T&K dynamics, but they were not identified as such there.

Instabilities accompanying KHI driving turbulence and mixing exhibit diverse forms, scales, and effects that depend on the initial Richardson, Reynolds, and Prandtl numbers: *Ri*, *Re*, and *Pr*, respectively. Early idealized analytic and three-dimensional (3D) modeling studies of KHI at low resolution revealed the emergence of secondary CIs within the billow cores (e.g., Klaassen & Peltier, 1985, 1991; Palmer et al., 1996, 1994; Werne & Fritts, 1999). A large literature thereafter explored secondary CI and KHI responses for varying *Ri*, *Re*, and *Pr* in oceanic and atmospheric applications (e.g., Mashayek & Peltier, 2012a, 2012b; Fritts, Baumgarten, et al., 2014; Fritts et al., 2013). Despite early laboratory studies revealing KHI T&K dynamics and subsequent evidence of likely KHI T&K events in lower atmosphere cloud layers by Thorpe (2002), no modeling addressing these dynamics was performed until that by Fritts, Wang, Lund, et al. (2022) motivated by the observations by Hecht et al. (2021). A subsequent initial direct numerical simulation (DNS) of T&K dynamics and energetics was described by Fritts, Wang, Lund, et al. (2022) and Fritts, Wang, Thorpe, et al. (2022). These modeling studies revealed T&K dynamics to be dramatically stronger, and more complex and energetic, than the secondary CI and KHI of individual KH billows that have been the focus of modeling for ∼30 years.

This paper presents imaging and interpretation of several types of instability transitions and dynamics leading to turbulence observed accompanying KHI T&K events during the Polar Mesospheric Cloud Turbulence (PMC Turbo) experiment performed aboard a stratospheric balloon that flew from Esrange, Sweden to northeastern Canada during 6 days in July 2018 (Fritts et al., 2019). Our paper is structured as follows. Section 2 provides a brief overview of the instruments, image processing techniques employed here, and the tracer attributes of PMCs. An overview of KHI secondary CI, KHI, and T&K dynamics employing the modeling described by Fritts, Wang, Lund, et al. (2022) is provided for reference in Section 3. Sections 4 and 5 describe the PMC profiles obtained by the Rayleigh lidar and the imaging revealing the KHI T&K dynamics, respectively. Section 6 discusses the implications of these observations and their relations to previous studies. Our summary is presented in Section 7.

2. Instruments and Observation Details

2.1. Instrument Overview

The PMC Turbo payload included seven optical cameras, each of which was contained within a pressure vessel. Three pressure vessels included narrow-field lenses that provided a $10° \times 15°$ field of view (FOV), at a spatial resolution of approximately 3 m per pixel at the PMC layer. The remaining four pressure vessels included wide-field lenses with a $25° \times 40°$ FOV and a spatial resolution of 8 m per pixel at the smallest off-zenith angles in the FOV. The spatial resolution of the wide-field cameras decreased with increasing off-zenith angle in the FOV to 18 m per pixel, not including motion blur. The reduced FOV of the narrow-field cameras reduced the change in resolution across their images. All cameras recorded monochrome images and included a 600 nm high-pass red filter to increase the signal-to-noise ratio of PMCs by preferentially removing Rayleigh scattering. Images recorded by the wide-field cameras are used for the analysis in this paper since the higher resolution of the narrow-field cameras is not necessary to resolve the smaller-scale features observed in the KHI analyzed in this paper.

The focus for these lenses was initially set at infinity, but was checked periodically by sweeping a narrow range of focus steps and examining the spread of point sources (stars) within the images captured during the sweep. In general, exposure times were set by a custom auto-exposure algorithm which automatically adjusted exposure

every few seconds such that the image statistics met adjustable parameters. The exposure could be manually set as well. Images were captured in burst exposures of 2–4 roughly every 2 s. The number of images in each burst was determined by the exposure selected by the auto-exposure algorithm. PMC Turbo imaging captured large spatial scales from ∼10 to 100 km, instability dynamics at scales of ∼1–10 km, and fine structure approaching the inner scale of turbulence at ∼20 m.

In addition to the seven optical cameras, the PMC Turbo payload included a high-power, high-resolution Rayleigh lidar. The Balloon Lidar Experiment (BOLIDE) provided continuous vertical profiling of the PMC layer at a 28° zenith angle within the FOV of the central cameras, all of which viewed in the anti-sun direction. BOLIDE operated at 532 nm and collected the photons from Rayleigh backscatter in the atmosphere by Mie backscatter from PMC ice particles using a 0.5-m-diameter telescope. BOLIDE soundings of the PMC layer employed spatial and temporal resolution of 20 m and 5 s, respectively. The lidar profiling complemented the PMC imaging enabling a quasi-3D characterization of GW and instability dynamics revealed in the PMC layer.

The PMC Turbo payload launched from Esrange, Sweden on July 8, 2018 and landed virtually undamaged in western Nunavut, Canada on 14 July. Image analysis of the data retrieved from the PMC imagers began with a standard flat-fielding procedure outlined in Fritts et al. (2019). Images were projected onto a plane at the PMC altitude to remove the distortion due to viewing geometry and find the correct scales and shapes of the observed dynamics. The volume backscatter coefficient of PMC particles (a measure of PMC brightness) was derived from lidar soundings by comparison of the backscatter signal to a standard atmosphere density profile after background subtraction and correction for the slanted beam and gondola float altitude. PMC Turbo instruments and preliminary analysis methods are described in greater detail in two PMC Turbo instrument papers (Kaifler et al., 2020; Kjellstrand et al., 2020), and in the C. B. Kjellstrand (2021) and C. Geach (2020) theses, as well as by Kaifler et al. (2022a, b, submitted to ESSD).

2.2. PMC Tracer Attributes

In this analysis, we assume that the dynamics are evolving on a sufficiently rapid time scale that the ice particles that make up the PMCs maintain their radius. As anticipated in airglow analysis of KHI (Fritts, Wan, et al., 2014) and previous observations of KHI in PMCs from the ground (Baumgarten & Fritts, 2014), this implies that brightness is conserved following an air parcel (for small vertical excursions) and the PMCs can thus be considered a passive tracer of large- and small-scale motions. Where PMC brightness occurs in very thin layers, as noted by Fritts et al. (2019) and will be seen below, these layers are very sensitive to small-scale instabilities and turbulence and reveal their evolution on time scales from minutes to seconds.

3. Overview of KHI T&K Dynamics

The KHI T&K dynamics that are the subject of this study are illustrated for reference using the modeling described in the initial paper by Fritts, Wang, Lund, et al. (2022). As described there, the KHI field was simulated using the Complex Geometry Compressible Atmosphere Model (CGCAM) to describe the interactions of mis-aligned KH billows specified to impose a region in which two billow cores link to three billow cores along their axes, or two billow cores link to one, such as observed by Hecht et al. (2021) and seen to arise at several sites in this study. The CGCAM domain configuration and initial conditions are described by Fritts, Wang, Lund, et al. (2022), hence are not repeated here.

3D imaging of the KHI T&K vortex dynamics are shown in Figure 1 at two times separated by $\sim 0.4T_b$, for a buoyancy period T_b at the initial shear layer. These features are displayed using the parameter λ_2, which described rotational, rather than shear causes of vorticity (Jeong & Hussain, 1995; see Fritts et al., 2021; Fritts, Wang, Lund, et al., 2022, for details). λ_2 is a non-dimensional eigenvalue, with large magnitudes representing strong rotation shown with red orange-colors in Figure 1. The times shown are after initial KHI T&K interactions and include the following elements:

1. Emerging KH billow cores at two locations at left and three locations at right (green labels in panel a).
2. Strong, large-scale vortex tubes (red labels in panel a).
3. Links of tubes and KH billow cores in three “knot” regions (yellow labels in panel a).
4. Emerging secondary KHI on the intensifying vortex sheets between adjacent KH billows, and largely parallel to the KH billow cores at early times (orange labels in panel a), and

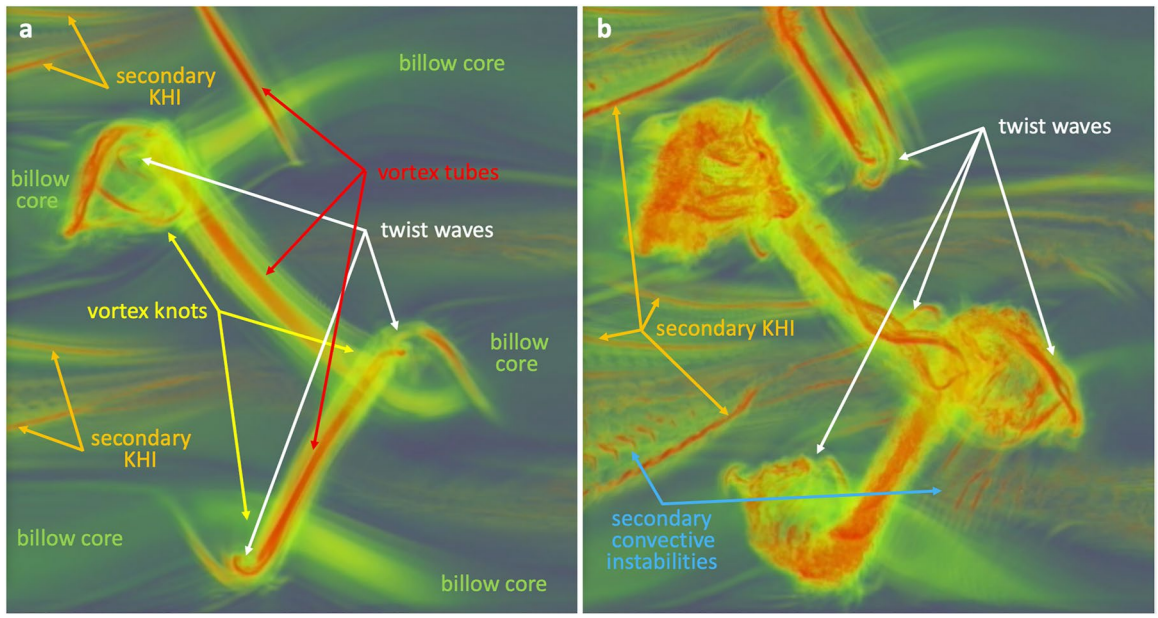

Figure 1. Examples of Kelvin-Helmholtz instability (KHI) "tube and knot" (T&K) dynamics of mis-aligned KH billows (see text for details).

5. Initial Kelvin (1880) vortex waves, or "twist" waves, that are excited where roughly orthogonal vortices interact in close proximity (white labels in panel a; see Arendt et al., 1997; Fritts et al., 1998, Fritts, Wang, Lund, et al., 2022).

   Panel b of Figure 1 reveals these dynamics to evolve rapidly over the next ~0.4T_b. Additional and/or evolved features include the following:

6. Further evolved and intensifying secondary KHI (orange labels in panel b).
7. Emerging secondary CIs in the outer KH billows (blue labels in panel b), and
8. New and further evolved twist waves at small and large scales (white labels in panel b).

4. Observations

4.1. KHI Billows in Large-FOV Images and Lidar Profiling

The KHI events discussed in this paper were observed on July 12, 2018 between 13:25 and 13:40 UT when PMC Turbo was located at ~68°N, 72°W above Baffin Island, Canada. During this time, strong KHI were widespread in the PMC layer across a ~50 × 100 km section of the sky. The bright KHI are shown in the left half of the projected FOV in Figure 2. The mean KHI wavelength was measured by performing a spanwise average of the PMC brightness at the inferred orientation of the band of KHI. The mean separation between peaks of the spanwise average was found to be 5.2 ± 2.5 km. The KH were advected from Southeast to Northwest at ~75 m/s and were oriented roughly perpendicular to the direction of advection. Also seen in Figure 2 is a tendency for KH billows to exhibit the most coherent (and brightest) amplitudes in bands (oriented from upper right to lower left in Figure 1) roughly orthogonal to the KH billow axes and exhibiting spatial variations along the KH billow axes at ~10–30 km scales.

Additional quantitative information on the structure, evolution, and dynamics of the KHI event is provided by the PMC Turbo Rayleigh lidar profiling of the PMC layer. Figure 3a shows a 7-hr profiling sequence that exhibits

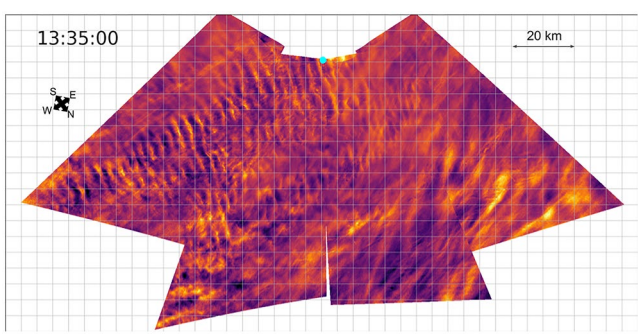

Figure 2. Projected images from the four wide field of view (FOV) PMC Turbo cameras. Images from the four wide-field cameras were obtained at 13:35:00 UTC, at 68°N, 72°W (above Baffin Island). The images have been projected as if viewed from below. The cyan dot indicates the approximate location of the Rayleigh lidar beam. The color scale of this image is linear, and ranges from purple to yellow with increasing brightness.

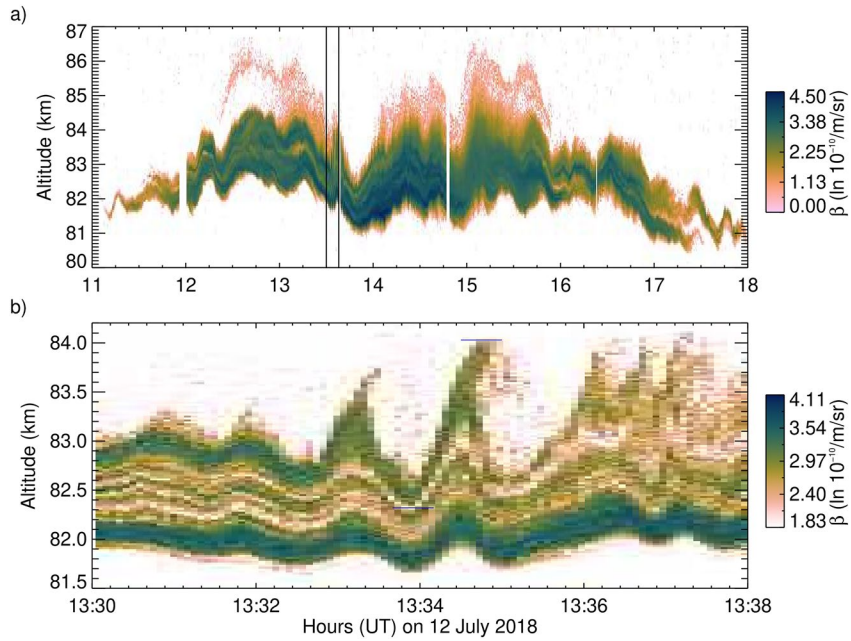

Figure 3. Altitude-time sections of the PMC layer sounded by lidar between (a) 11 and 18 UTC on July 12, 2018 at 60 m and 30 s resolution, and (b) 13:30 and 13:38 UTC at 20 m and 5 s resolution. Larger-scale gravity wave (GW) signatures with periods of ∼20 and ∼60 min are visible in the highly variable PMC layer shown in (a), while the zoomed view in (b) shows a fine-scale, multiply layered PMC with prominent signatures of vertical displacements—the two strongest on 13:33:17 and 13:34:38 UT—that we identify as due to Kelvin-Helmholtz (KH) instabilities. The two blue horizontal line segments indicate a vertical displacement of the top layer around 13:34:38 UT of 1.7 km.

peak-to-peak vertical excursions of ∼1.5 km at the lower edge and as large as ∼4 km at the upper edge. The larger excursions at lower and higher altitudes are caused by GWs having observed periods of ∼2 hr and longer. Additional GWs having observed periods of ∼10 min to 1 hr contributed smaller displacements throughout the PMC layer. GW displacements, δz, of the PMC brightness layer to above or below its equilibrium altitude imply GW vertical wavelengths $\lambda_z \sim 2\pi\delta z$ or larger, assuming that GWs cannot sustain amplitudes larger than required for overturning (see Fritts et al., 2017). The superpositions of GWs with a variety of scales leads naturally to local shears attaining sufficiently small *Ri* to initiate KHI. The KHI apparent in Figure 1 spans over 100 km. While we cannot definitively identify the source of the shear leading to KHI spanning this distance, it is plausible that a large-scale GW caused the shear, since we observe evidence of such GWs in the vertical perturbations of the PMC layer.

We therefore theorize an environment resulting from GWs of several scales. As noted, larger scale (>100 km λ_h) GW likely led to the shear required to form KHI. Smaller GWs (∼20 km λ_h) modulated *Ri* and *Re*, leading to the fluctuations in KHI coherence noted in Figure 2. This theory is supported not only by our PMC images in Figure 2 and lidar backscatter traces in Figure 3, but also by the temperature fluctuations measured by the Rayleigh lidar at lower altitudes. These temperature fluctuations are described in depth in Fritts et al. (2019) in Section 2.2.2 and Figure 6. The lidar instrument and data is described in depth in Kaifler et al. (2020).

The zoomed lidar profiling sequence (Figure 3b) shows very short-period, distinct modulations of the PMC layer and increased PMC backscatter where the layer modulation is maximum that we identify as due to KHI. The induced maxima in vertically integrated PMC brightness occur at 13:33:17 ∼ UT and 13:34:38 ∼ UT with a difference of 1.5 min. Both the times of detection and the temporal separation coincide with the detection of KHI billows in the PMC imaging discussed above. The observed PMC layer displacements reveal characteristics of the KH billows, specifically their depths and their direction of rotation, the latter of which reveals the underlying wind shear in the plane normal to the KH billow axes.

From our lidar traces (Figure 3b), we see that the largest displacement of the top PMC layer from 13:34 to 13:36 UTC exhibits a lower edge at ∼82.3 km and an upper edge at ∼84 km (marked by short blue horizontal

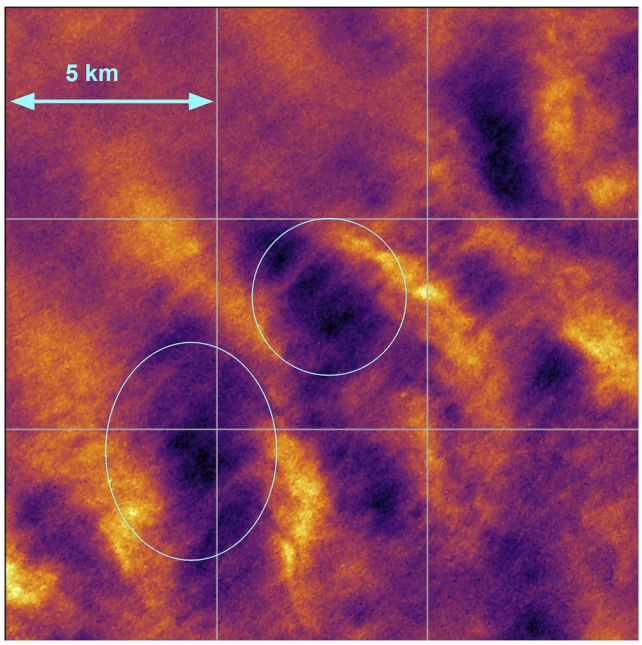

Figure 4. A 15 × 15 km projected section of the sky at 13:35:50 UTC. Highlighted regions show numerous filaments believed to be convective instabilities within successive Kelvin-Helmholtz (KH) billow cores.

lines in Figure 3b), which we interpret as a billow depth of ∼1.7 km. We observe a ratio of depth to λ_h of approximately 0.32 for λ_h = 5.2 km implying $Ri \sim 0.1$, based on detailed laboratory studies (Fritts & Rastogi, 1985; Thorpe, 1973a, 1973b—see especially Figure 3 and accompanying discussion). From theory, observations, and modeling we infer from the KH billow wavelength an approximate half shear depth of $h \sim \lambda_h/4\pi \sim 400$ m. Previous observations suggest a maximum shear layer $N_{max} \sim 0.028$ s^{-1} and scaling the kinematic viscosity ν_0 at the surface of the Earth with the decrease in fluid density with altitude, we estimate $\nu_0 \sim 1.8$ m^2/s. From these values, we estimate $U_0 \sim Nh/Ri^{1/2} \sim 35$ m/s and $Re = U_0 h/\nu_0 \sim 7{,}900$.

Referring to the image of the PMC layer in Figure 2 at this time, however, we see that the KHI were clearly less intense at the location of the lidar profiling than at the sites of strongest KHI dynamics ∼30–50 km farther off-zenith to the lower left that are our analysis foci in this paper. These apparent KHI intensity differences suggest significantly stronger KHI, deeper billows yielding larger brightness contrast across their phases, and implied stronger shears and smaller initial *Ri*, perhaps smaller by 2–3 times at our analysis sites. $Ri \sim 0.03$ would suggest $Re \sim 13{,}600$. These ballpark estimates were used in the initial modeling of KHI described in our companion paper (Fritts et al., 2022, Multi-Scale Kelvin-Helmholtz Instability Dynamics Observed by PMC Turbo on 12 July 2018: 2. Modeling KHI Dynamics and PMC Responses, Submitted September 2021).

The lidar trace shown in Figure 3b also reveals that the billows rotate clockwise. In the profiling cross-section, the left edge of the billow is the first region to be advected through the lidar beam, given the near-zenith position of the beam (marked with a cyan dot in Figure 2) and the observed mean wind to the Northwest. We observe the PMC layer increasing in altitude as it moves through the beam. This implies a KH shear layer that has a large-scale wind in the plane orthogonal to the KH billow axes that increases toward zenith with increasing altitude.

Advection of the bright PMC layer upward at the left edges of the KH billows seen in Figure 3b implies increasing of the vertically integrated brightness in these regions, enhanced visibility of smaller-scale features in these regions, and the opposite where less bright PMCs are advected downward (see the airglow modeling by Fritts, Wan, et al., 2014, Figure 7). The effect is to shift high-brightness sensitivity toward the "upstream" side of the KH billows and cause the region of downward entrainment to be less bright by comparison.

From lidar profiling of PMCs during the KHI event, we observe that the top of the KHI is near or above the maximum upward extent of the PMC layer. The upper portion of a KH billow entrains air from above the PMC layer and moves it into the brighter regions, reducing the density of ice particles and therefore reducing integrated brightness. Simultaneously, the lower regions of a KH billow increase ice particle density in the edges, increasing integrated brightness. The consequences are brighter leading (rising) edges, darker trailing (descending) edges (see Figure 1 in Fritts, Wan, et al., 2014, for example), and peak PMC brightness shifted toward the leading edges of the KH billows.

4.2. CI Rolls Associated With KHI

Bright PMC filaments running perpendicular to KH billows are common during the period of strong KHI from 13:25 to 13:40 UTC. The filaments are seen to occur within the darker KH billow cores as they achieve large amplitudes (indicated by strong brightness variations at primary KH billow scales seen in Figure 4). The cyan circles in Figure 4 highlight two regions with relatively brighter PMCs due to upward advection by the KH billows at their leading edges, as discussed above. The filaments in Figure 4 extend lengthwise across the entire KH billows, ∼5 km.

The dynamics and morphology of these filaments are consistent with convective rolls. Convective rolls become visible because they occur where there is a strong vertical gradient in PMC brightness and differential vertical advection between adjacent rolls yield variable brightness across the convective rolls when viewed from below, as

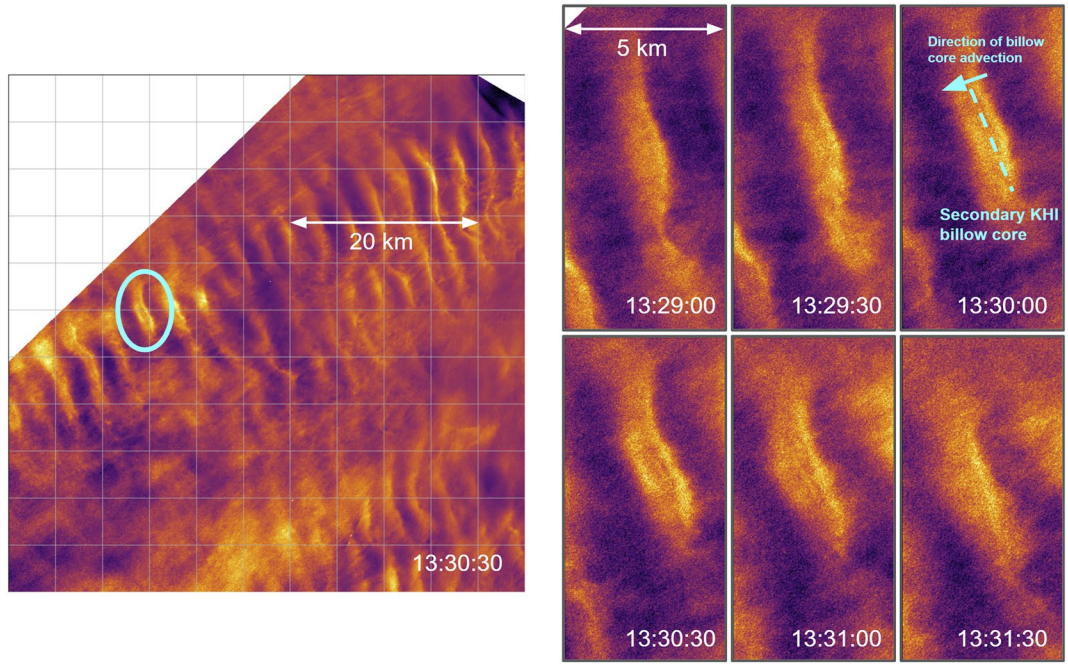

Figure 5. Dark structures associated with secondary Kelvin-Helmholtz instability (KHI) are apparent within primary KH billow leading edges in an image section obtained at 13:30:30 on July 12, 2018 (shown at left). The temporal evolution of the billow highlighted with a cyan circle is shown to the right. The KHI is advected according to the arrow shown at 13:30:00 UT. Note that the dark feature is advected through the billow.

modeled by Fritts, Wan, et al. (2014). It is clear from the lidar traces in Figure 3 that the PMCs we examine in this paper do have a strong vertical gradient in brightness. The filaments are observed to form perpendicular to KH billows, which is consistent with our models (Fritts et al., Multi-Scale Kelvin-Helmholtz Instability Dynamics Observed by PMC Turbo on 12 July 2018: 2 Modeling KHI Dynamics and PMC Responses, Submitted September 2021).

As seen in Figure 4, the spatial scales and intensities of CIs are not uniform along the length of the billow cores. Furthermore, the coherence of the KHI varies across the composite FOV shown in Figure 2. As discussed in Section 4.1, we attribute these variations to inhomogeneities in the initial shear layer, background turbulence, and modulation by GWs, all of which could cause variations in Ri and Re along the billow axes at the time of KHI initiation. Their timescales are likewise dependent on initial conditions and their intensities, but they appear to remain coherent for ~2–3 min prior to exhibiting a transition to smaller-scale turbulence.

4.3. Secondary KHI

During several periods of intense KHI, we observe dark features within the brighter leading edges of KH billows. These features are largely parallel to the KH billow cores and move past the billow edges over the course of a few minutes. Their scales are much smaller than the KH billow wavelengths. The left panel of Figure 5 shows a 55 × 55 km area of the FOV and exhibits several KH billows, each of which includes the formation of the dark structures. The panels on the right side of Figure 5 follow the development and motion of one of the dark features relative to a single KH billow as it advects across the sky. In the first panel of this sequence (13:29:00), the dark features are not yet visible within the KH billow edge. As time passes (noted in the panel timestamps), the feature is visible and moves from upstream (right) to downstream (left). The movement of the dark feature is consistent with the air motion associated with the primary KH billow core. By the final panel, the feature has either moved past the edge or dissipated and is no longer visible.

Secondary KHI form on the strongly sheared layers between adjacent KH billows and are advected around the primary billows as they rotate. Secondary KHI have significantly smaller spatial scales than the primary KH billow because their wavelengths and depths are dictated by the much thinner intensified vorticity sheets between

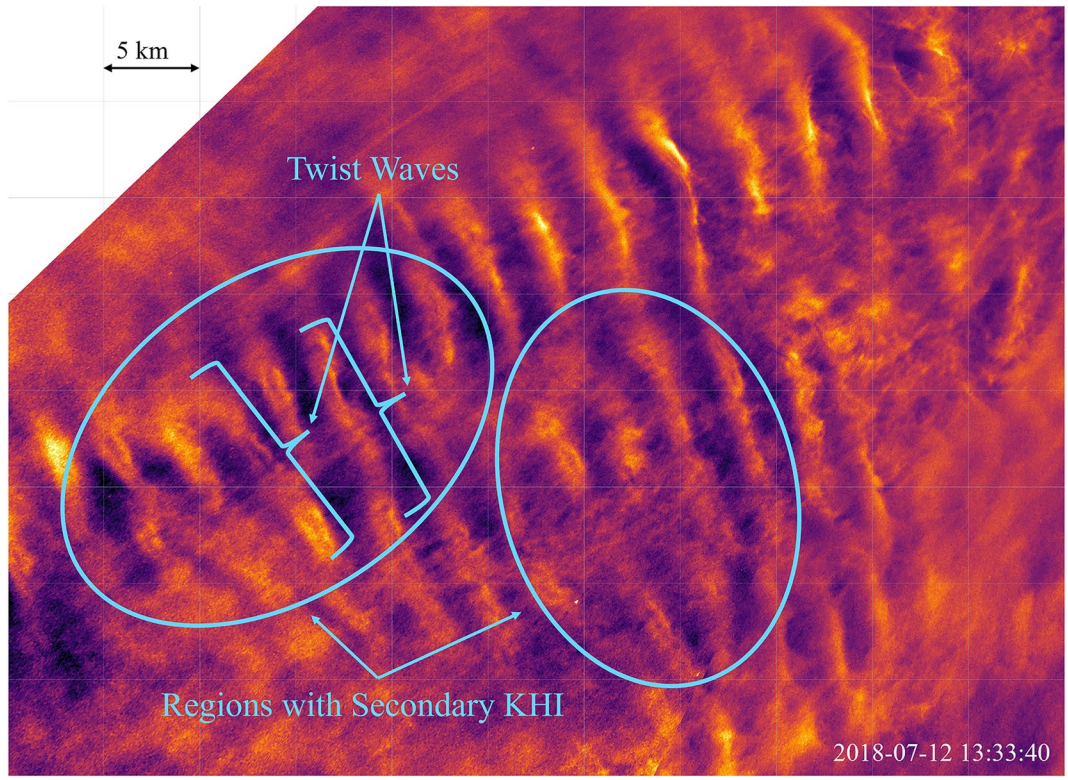

Figure 6. A larger scale view of secondary Kelvin-Helmholtz instability (KHI) forming on almost every KH billow across the total field of view. Regions with secondary KHI and individual twist waves have been marked.

the primary billows (e.g., $\lambda_h \sim 4\pi h$, for h the half-depth of the intensified vorticity sheets). Secondary KHI are also expected and observed to be oriented largely parallel to the primary KH billows and to exhibit significant horizontal extents along the primary KH billows because the vorticity sheets that provide their sources have vorticity largely aligned with the primary billows. Therefore, the behavior, morphology, and advection of these dark features are all consistent with secondary KHI. Furthermore, modeling in our companion paper confirms that secondary KHI traced by PMCs match the observations shown in Figure 5 (Fritts et al., 2022, Multi-Scale Kelvin-Helmholtz Instability Dynamics Observed by PMC Turbo on 12 July 2018: 2. Modeling KHI Dynamics and PMC Responses, Submitted September 2021).

Modeling of interacting KHI at sufficiently high *Re* to aid interpretation of these KHI observations provides evidence that the *Re* and *Ri* we infer from our observations (outlined in Sections 4.1) will result in strong primary KHI and secondary KHI (Fritts et al., Multi-Scale Kelvin-Helmholtz Instability Dynamics Observed by PMC Turbo on 12 July 2018: 2. Modeling KHI Dynamics and PMC Responses, Submitted September 2021). Specifically, secondary KH billows arise where the primary KH billows evolve in isolation and where they undergo KH billow interactions leading to T&K dynamics. Because adjacent primary KH billow induce advection along the intensified vorticity sheet between them, secondary KHI advection is away from the stagnation point at this shear layer and between primary KH billows, hence upward, rightward, and upstream (downward, leftward, and downstream) over the right (left) KH billow in each case for the orientations shown in Figure 5.

Without considering the PMC brightness gradient, we would expect to observe secondary KHI on the upstream and downstream edges of the primary KHI. However, the KHI layer we observe is located above the maximum brightness in the PMC brightness gradient. Therefore, we anticipate ascending secondary KHI advecting downstream over the bright upwelling region over the downstream KHI billow. Since this region is already bright, the ascending secondary KHI does not appreciably change the brightness. Conversely, the descending secondary KHI advecting upstream occurs over the bright descending region under the upstream KH billow, and we do anticipate an appreciable decrease in brightness and leftward advection. Our observations match these predictions.

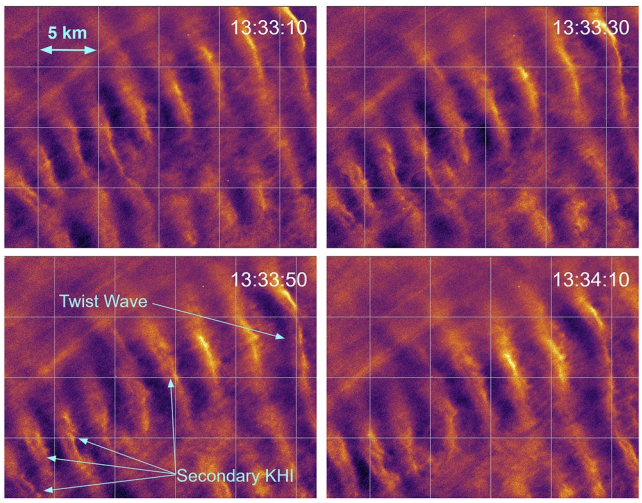

Figure 7. Numerous examples of secondary Kelvin-Helmholtz instability (KHI) and twist waves.

We find no other plausible dynamics that explain the systematic formation of dark features parallel to primary KH billows having much smaller widths. Hence, we conclude that the narrow, dark features aligned along the primary KH billow axes must be secondary KHI.

Secondary KHI is also observed in images from 13:33 to 13:37, several of which are shown in Figures 6 and 7. The secondary KHI at this time is more widespread across the region of relatively more intense KHI. It is common in our observations that a secondary KH billow progresses at different rates along the secondary KH billow core axis. While these events are nearly contemporaneous to the events shown in Figure 4, they occur some 40 km away. We also observe KH billows undulating in the x-y plane along the billow core axis, which is consistent with the behavior of twist waves.

In Figure 7, the secondary KHI aligned along the billow is seen to be advected around the primary KH billow at rates varying along the axis of the secondary billow. Several secondary KH billows demonstrating this behavior are noted in the third panel of Figure 7. The differential progression of the secondary KHI along the primary KH billow axis must be a result of differential primary KH billow rotation along the length of the billow core.

4.4. KH Billow Interactions

During the periods of intense KHI examined in this paper, we observed numerous KH billow interactions. One example is shown in Figure 8. In the top left panel, there are two KH billow cores that appear to be interacting strongly. The location of the billow interaction is highlighted with the cyan circle in each panel. The interacting billows are advected together across the FOV over the course of the 2 min shown in the figure. Initially, the rightmost billow terminates, traced by the meeting of the surrounding billow edges in a chevron pattern. In the 13:29:50 panel, we see evidence of interaction with the left billow. Near the point where the two billows interact, there are complex features evolving into small-scale turbulence. Two brighter streaks connect the leftmost billow edge to the center edge and the right edge. While we see evidence of CIs throughout the image, the interactions between billows can be distinguished from CIs by their more chaotic shape which is not aligned perpendicular to the KH billows. In the top right panel, at 13:29:20, the sharp edges of the billows on the left side of the right billow evolve from a firm boundary to become more diffuse. Both the left and right billow terminate, and the turbulence intensifies and exhibits complex structures. While the turbulent features were initially localized to the region of billow interaction, by 13:29:20, turbulence features have extended several kilometers away from the merging point along the billow axes. In the lower right panel, at 13:30:20, the left billow develops along the right side reminiscent of the terminating edge of the right billow at 13:28:50. The right billow core becomes more continuous, although a kink forms near the location of the original billow termination. At the end of the event shown in Figure 8, remnants of the turbulence exist throughout the merging billows, but the turbulence is less intense and many of the remaining features are more ubiquitous CIs.

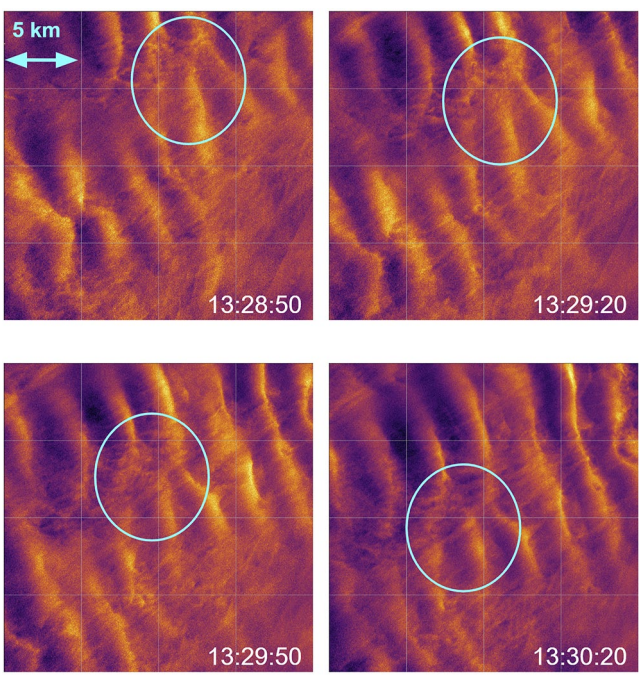

Figure 8. Panels show the evolution of a 20 km by 20 km section of the sky containing billow interactions.

"Z" and "W" patterns are apparent in regions "a" and "c" of Figure 10. In region "b" we see several billows interacting and forming a region of strong turbulence. A localized region of interest is examined over several minutes in Figure 9. Figure 9 shows the evolution of a "W" pattern similar to the billow interaction imaged in Figure 8. However, while the billows in Figure 8 first terminate, but become more continuous, the interacting billows in Figure 10 become less cohesive. At 13:28:40 UTC, the billows are well-defined, but 30 s later turbulence has formed between them. At 13:29:40 UTC, turbulent structures continue to develop. Brighter regions of PMCs connect the fraying

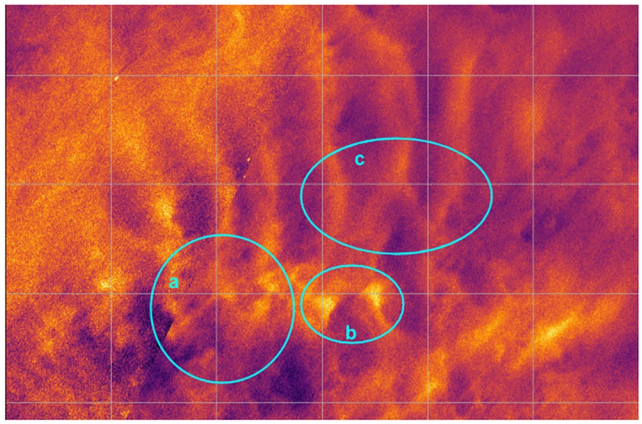

Figure 9. Multiple interactions between billows are present along with knots and other instabilities at 13:29:10 UTC.

KH edges. There is more widespread turbulence present as well, suggesting that knots are breaking down into smaller scale turbulence. The following 2 min continue the trend towards turbulence, and by the final set of billows at 13:31:40 UTC the billow cores are no longer coherent.

The dynamics observed in Figures 8–10 closely match adjacent KH billow merging T&K events produced in the laboratory (Schowalter et al., 1994; Thorpe, 1985) and billow interactions modeled through DNSs (Fritts et al., Multi-Scale Kelvin-Helmholtz Instability Dynamics Observed by PMC Turbo on 12 July 2018: 2. Modeling KHI Dynamics and PMC Responses, Submitted September 2021). The "W" and "Z" patterns are consistent with KH billows interacting via T&K. The bright streaks between KH billow edges are consistent with the predicted entrainment of PMC ice particles by vortex lines which form tubes between interacting billows. The turbulent regions at the locations of billow interactions closely match the entanglement of these vortex lines into knots. The billow interactions observed dissipate into a less cohesive structure within minutes of the beginning of the interactions, which is also consistent with the observed and modeled lifetimes of knots. Therefore, we believe these events provide an example of KHI dissipating into turbulence through the formation of knots and tubes during interaction between billows. The KH billows dissipated on a timescale of roughly 3 min and the spatial scale of the knots was 1–5 km. For more information regarding the similarities between the billow interactions observed by PMC Turbo and KHI models including billow interactions, refer to our companion modeling paper (Fritts et al., 2022, Multi-Scale Kelvin-Helmholtz Instability Dynamics Observed by PMC Turbo on 12 July 2018: 2. Modeling KHI Dynamics and PMC Responses, Submitted September 2021).

5. Discussion

KH instabilities and the turbulence and mixing they induce play major roles in energy dissipation and in defining vertical structure and variability through the atmosphere, oceans, and other stratified and sheared geophysical fluids (Rosenberg & Dewan, 1975; Sato & Woodman, 1982; Woodman & Rastogi, 1984; Woods, 1968; Woods

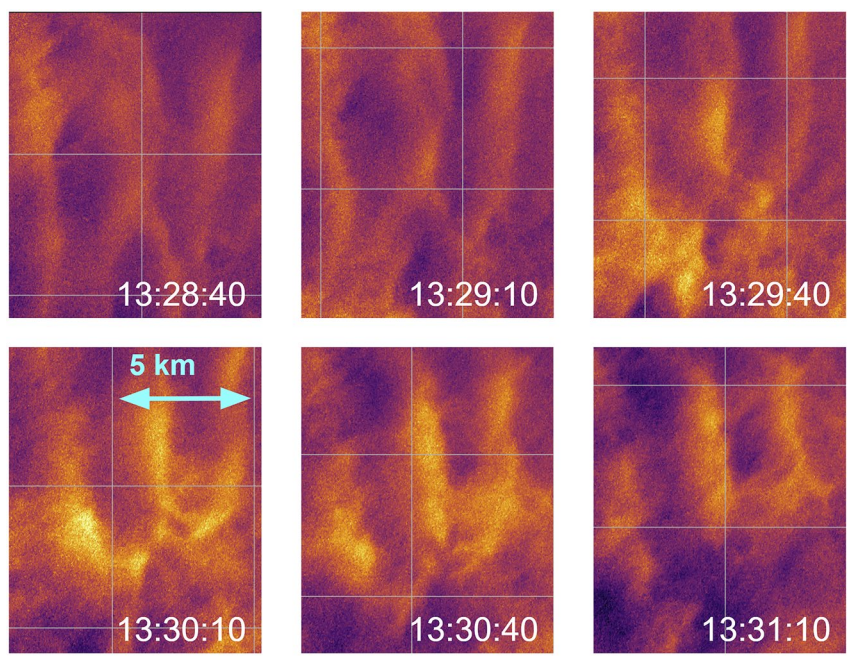

Figure 10. Evolution of one Kelvin-Helmholtz (KH) billow interaction tracked at a 30 s cadence exhibiting merging billows. This region is shown in Figure 8 in region "c".

& Wiley, 1972; also see the extensive reviews by Thorpe, 1987, 2002, and additional references therein). The importance of specific events depends on their scales, the environments in which they arise, and the character and intensities of secondary instabilities driving their turbulence transitions.

The scale of the observed features' wavelength allows us to identify the instabilities as accompanying KHI rather than GWs. Distinctions between instabilities accompanying KHI and GW breaking arise due to their very different horizontal wavelengths, λ_h, accounting for instabilities, and their different instability character. At the $\lambda_h \sim$ 5-km scales of relevance in this study, GWs are almost certainly ducted or evanescent in the MLT, or have much smaller vertical wavelengths, λ_z, because their vertical propagation requires a finite λ_z, and real $m = 2\pi/\lambda_z = k(N^2/\omega_i^2 - 1)^{1/2}$, for vertical (horizontal) wavenumber m (k), buoyancy frequency N, GW intrinsic frequency $\omega_i = k(c - U_h)$, and c and U_h the GW phase speed and mean wind along the GW propagation direction. But large and variable mean winds readily imply $|\omega_i| > N$ such that m is imaginary and the GW is locally evanescent. Larger GW c can more easily ensure real m, but typically requires GW $\lambda_h \sim$ 20 km or larger in the MLT. Thus, smaller GW λ_h are typically ducted, especially at scales as small as 5 km, and ducted GWs do not exhibit small-scale shears or regions of overturning that would initiate smaller-scale instabilities leading to turbulence.

Results presented here have provided quantitative insights into the diversity of KHI dynamics that arise in an environment exhibiting strong GW modulations and enabling energetic KHI at sufficiently large scales to attain a small *Ri* and large *Re*. We expect such events to be fairly common in the MLT, given the importance of small-scale GW breaking leading to energy and momentum deposition and the often significant large-scale shears in which these dynamics occur. While we observed KHI directly, we see strong evidence for modulation of the KHI initiation by GWs with periods ranging from ∼15 min to a few hours since KHI intensities exhibited horizontal variability at scales of ∼15 km and larger. Our modeling team took advantage of these observations to ensure their simulation results (described in the companion modeling paper) matched observations of nature.

Secondary instabilities in finite-amplitude KH billows have been observed in the atmosphere, oceans, and laboratory for over six decades, and they exhibit a wide diversity of forms, several of which have been quantified only recently (Baumgarten & Fritts, 2014; Browand & Winant, 1973; Caulfield et al., 1996; Hecht et al., 2014; Schowalter et al., 1994; Thorpe, 1971, 1973a, 1973b, 1985, 1987, 2002; Witt, 1962). At low *Re*, the only apparent instabilities of spanwise-uniform individual KH billows are convective rolls having large spanwise and temporal scales (Klaassen & Peltier, 1985; Palmer et al., 1996, 1994). These scales decrease and the convective rolls occur nearer the outer edges of the billows with increasing *Re* and decreasing *Ri* (Fritts, Baumgarten, et al., 2014; Fritts, Wan, et al., 2014; Thorpe, 1987; Werne & Fritts, 1999). Secondary KHI arising in the stratified braids between adjacent billows were seen previously in the oceans and laboratory and in more recent high-resolution modeling at higher *Re* and low *Ri* (Fritts, Baumgarten, et al., 2014; Fritts et al., 2019; Thorpe, 1987). Until recent airglow observations (Hecht et al., 2021), secondary KHI were not documented in atmospheric observations at any altitude. The high-resolution observations of secondary KHI shown in this paper help to place a qualitative constraint on the minimum *Re* for these other recent observations, and previous observations will benefit from further analysis incorporating these new conclusions.

Other instabilities arise where larger-scale motions cause inhomogeneities in the underlying shears inducing KHI. Where KH billow axes are nearly continuous, but billow cores exhibit variable rotation rates or spatial modulation, they evolve perturbations that are large-scale manifestations of Kelvin "twist" waves, which can act to fragment the billow cores thereafter (Arendt et al., 1997; Baumgarten & Fritts, 2014; Kelvin, 1880). Where such perturbations yield close spacings between adjacent billows, they can also lead to local vortex pairing (see Thorpe, 1987). Such modulations are widespread in KHI observations (Hecht et al., 2005, 2014) and suggest that these dynamics are likely to contribute to KHI breakdown and turbulence in general shear flows influenced by GW motions.

The companion modeling paper shows simulations including T&K resulting from vortex pairing by design. However, the unstable conditions required to allow such dynamics also leads to several classes of secondary instabilities organically. Figure 2 in the companion paper shows images from the same event described in depth in this paper, and highlights vortex tubes, secondary KHI, and CIs, just as we have examined in this paper. The same instabilities manifest in the simulation of T&K dynamics, and these instabilities have been highlighted in Figures 5–7 and 9 of the companion modeling paper.

In this study, we have identified cases of T&K arising from the interactions among adjacent KH billows having small *Ri* and large *Re* and resolved by imaging of thin layers in the MLT. As with other instabilities discussed

above, T&K were seen in early laboratory shear flows (Thorpe, 1987) and argued by Thorpe (2002, especially Figure 12) to be expected and widespread in the atmosphere as well. PMC Turbo imaging offers a unique perspective on these dynamics because of its ability to define the evolution of very thin layers revealing very small features continuously in time for KHI events having much larger initial scales.

Our observations confirm Thorpe's expectations for such dynamics in the atmosphere, and parallel modeling (Fritts et al., Multi-Scale Kelvin-Helmholtz Instability Dynamics Observed by PMC Turbo on 12 July 2018: 2. Modeling KHI Dynamics and PMC Responses, Submitted September 2021) reveals that the dynamics of T&K are dramatically stronger than the secondary CIs and KHI within individual KH billows. Specifically, the accompanying modeling shows that knots arising from initial vortex tubes yield mean energy dissipation rates that are 2–5 times higher than the mean values accompanying KH billows exhibiting secondary CIs and KHI alone. These results are presented in Section 6.1 and illustrated in Figure 13 of the companion modeling paper.

Additionally, the ability to quantify the occurrence and scales of secondary CIs and KHI for individual KH billows enables an assessment of the influences of preexisting turbulence on the KHI evolution. Based on an inferred half shear depth, $h \sim \lambda_h/4\pi \sim 400$ m, and an inferred half shear horizontal velocity difference $U_0 \sim Nh/Ri^{1/2} \sim 35$ m/s, we expect a KHI $Re \sim 7900$–$13{,}600$. This implies very small secondary CI scales. The observed CI scales are ∼500 m or somewhat larger, suggesting instead an effective "turbulence" Reynolds number, $Re_{turb} = U_h/\nu_{turb} \sim 2{,}000$–$5{,}000$, where ν_{turb} is the effective turbulent kinematic viscosity due to preexisting turbulence. Additionally, the occurrence of secondary KHI in the braids between adjacent KH billows implies $Re_{turb} \sim 4{,}000$ or larger, based on the determination of the needed Re allowing secondary KHI for $Ri = 0.05$. Hence, the most likely value is $Re_{turb} \sim 4{,}000$–$5{,}000$, and implies a $\nu_{turb} \sim 1.6$–3.4 times larger than ν.

6. Summary

The utility of PMCs to act as sensitive tracers of small-scale GW and instability dynamics in the MLT has long been recognized (see Witt, 1962), but previous observations were limited either by the viewing geometry or the seasonal limitations imposed by ground-based observations. PMC Turbo was able to reduce the off-zenith viewing angle and the viewing distance, and continuously image dynamics revealed in the PMC layer under continuous daytime conditions, by suspending a viewing platform beneath a balloon floating at ∼37 km altitude. PMC Turbo high-resolution imaging from this platform resulted in identification and quantification of multiple instabilities contributing to the transition to turbulence of larger-scale KH billows, several reported for the first time. We observe secondary instabilities of primary KH billows including secondary KHI in the stratified bands between adjacent billows, which place lower limits for the primary KH billow Re, as well as interactions among adjacent KH billows having various forms and implications. Such interactions can lead to KH billow pairing and undulations of the billow axes exhibiting twist wave behavior, both of which can contribute to additional KH billow instabilities and transitions to turbulence. The most significant result of this analysis, however, was the identification and quantification of multiple cases of KH billow interactions leading to T&K identified previously in laboratory studies and suggested by billow clouds in the lower atmosphere. These dynamics were seen to be very vigorous and lead to rapid dissipation of the initial larger-scale KH billows in these regions. Parallel modeling of these dynamics reported by Fritts et al. (submitted 2021) reveal that the dynamics of T&K dramatically enhance the mean turbulence intensities and energy dissipation rates accompanying KH billow breakdown where it occurs.

While this study has focused on a single larger-scale KHI event, it demonstrates the potential for PMC Turbo high-resolution imaging and profiling (and related high-resolution imaging and profiling from the ground) to yield similar insights into other small-scale dynamics playing similar roles in the MLT, such as GW breaking and instability dynamics accompanying mesospheric bores (Fritts et al., 2020; Geach et al., 2020). More generally, the dynamics of small-scale GWs and instabilities leading to turbulence occur throughout the atmosphere but can only be observed continuously at scales extending from the GWs providing the energy and momentum inputs to the inner scale of turbulence (spanning ∼4 decades of scales) in the MLT. Thus, such PMC studies have the potential for scientific benefits throughout the atmosphere, in the oceans, and other geophysical fluids.

Data Availability Statement

PMC Turbo PMC images and videos, and BOLIDE lidar data can be accessed at the following link: https://halo-db.pa.op.dlr.de/mission/112. Refer to the supplemental materials for information about movies corresponding to Figures 4–10 hosted also accessible at the provided link.

Acknowledgments
The PMC-turbo mission was funded by NASA Contract 80NSSC18K0050 and supported by NSF grant AGS-2032678. This project also received funding from the German Aerospace Center (DLR) for construction, integration, and operation of the Rayleigh lidar and subsequent data analyses.

References

Arendt, S., Fritts, D. C., & Andreassen, O. (1997). The initial value problem for Kelvin vortex waves. *Journal of Fluid Mechanics*, *344*, 181–212. https://doi.org/10.1017/s0022112097005958

Baumgarten, G., & Fritts, D. C. (2014). Quantifying Kelvin-Helmholtz instability dynamics observed in noctilucent clouds: 1. Methods and observations. *Journal of Geophysical Research: Atmospheres*, *119*, 9324–9337. https://doi.org/10.1002/2014JD021832

Browand, F. K., & Winant, C. D. (1973). Laboratory observations of shear-layer instability in a stratified fluid. *Boundary-Layer Meteorology*, *5*, 67–77. https://doi.org/10.1007/BF02188312

Browning, K. A., & Watkins, C. D. (1970). Observations of clear air turbulence by high power radar. *Nature*, *227*(5255), 260–263. https://doi.org/10.1038/227260a0

Caulfield, C. P., Yoshida, S., & Peltier, W. R. (1996). Secondary instability and three-dimensionalization in a laboratory accelerating shear layer with varying density differences. *Dynamics of Atmospheres and Oceans*, *23*, 139–153. https://doi.org/10.1016/0377-0265(95)00418-1

Chau, J. L., Urco, J. M., Avsarkisov, V., Vierinen, J. P., Latteck, R., Hall, C. M., & Tsutsumi, M. (2020). Four-dimensional quantification of Kelvin-Helmholtz instabilities in the polar summer mesosphere using volumetric radar imaging. *Geophysical Research Letters*, *47*(1), e2019GL086081. https://doi.org/10.1029/2019gl086081

Fritts, D. C. (1984). Gravity wave saturation in the middle atmosphere: A review of theory and observations. *Reviews of Geophysics*, *22*(3), 275–308. https://doi.org/10.1029/RG022i003p00275

Fritts, D. C., & Alexander, M. J. (2003). Gravity dynamics and effects in the middle atmosphere. *Reviews of Geophysics*, *41*(1), 1003. https://doi.org/10.1029/2001RG000106

Fritts, D. C., Arendt, S., & Andreassen, Ø. (1998). Vorticity dynamics in a breaking internal gravity wave. Part 2. Vortex interactions and transition to turbulence. *Journal of Fluid Mechanics*, *367*, 47–65. https://doi.org/10.1017/S0022112098001633

Fritts, D. C., Baumgarten, G., Wan, K., Werne, J., & Lund, T. (2014). Quantifying Kelvin-Helmholtz instability dynamics observed in noctilucent clouds: 2. Modeling and interpretation of observations. *Journal of Geophysical Research: Atmospheres*, *119*, 9359–9375. https://doi.org/10.1002/2014JD021833

Fritts, D. C., Kaifler, N., Kaifler, B., Geach, C., Kjellstrand, C. B., Williams, B. P., et al. (2020). Mesospheric bore evolution and instability dynamics observed in PMC Turbo imaging and Rayleigh lidar profiling over Northeastern Canada on 13 July 2018. *Journal of Geophysical Research: Atmospheres*, *125*(14), e2019JD032037. https://doi.org/10.1029/2019JD032037

Fritts, D. C., Miller, A. D., Kjellstrand, C. B., Geach, C., Williams, B. P., Kaifler, B., et al. (2019). PMC Turbo: Studying gravity wave and instability dynamics in the summer mesosphere using polar mesospheric cloud imaging and profiling from a stratospheric balloon. *Journal of Geophysical Research: Atmospheres*, *124*, 6423–6443. https://doi.org/10.1029/2019JD030298

Fritts, D. C., & Rastogi, P. K. (1985). Convective and dynamical instabilities due to gravity wave motions in the lower and middle atmosphere: Theory and observations. *Radio Science*, *20*(6), 1247–1277. https://doi.org/10.1029/RS020i006p01247

Fritts, D. C., Wan, K., Werne, J., Lund, T., & Hecht, J. H. (2014). Modeling the implications of Kelvin-Helmholtz instability dynamics for airglow observations. *Journal of Geophysical Research: Atmospheres*, *119*, 8858–8871. https://doi.org/10.1002/2014JD021737

Fritts, D. C., Wang, L., Baumgarten, G., Miller, A. D., Geller, M. A., Jones, G., et al. (2017). High-resolution observations and modeling of turbulence sources, structures, and intensities in the upper mesosphere. *Journal of Atmospheric and Solar-Terrestrial Physics*, *162*, 57–78. https://doi.org/10.1016/j.jastp.2016.11.006

Fritts, D. C., Wang, L., Lund, T. S., & Thorpe, S. A. (2022). Multi-scale dynamics of Kelvin–Helmholtz instabilities. Part 1. Secondary instabilities and the dynamics of tubes and knots. *Journal of Fluid Mechanics*, *941*, A30. https://doi.org/10.1017/jfm.2021.1085

Fritts, D. C., Wang, L., Lund, T. S., Thorpe, S. A., Bjorn Kjellstrand, C., Kaifler, B., et al. (2022). Multi-scale Kelvin-Helmholtz instability dynamics observed by PMC turbo on 12 July 2018: 2. Modeling KHI dynamics and PMC responses, submitted September 2021.

Fritts, D. C., Wang, L., Thorpe, S. A., & Lund, T. S. (2022). Multi-scale dynamics of Kelvin–Helmholtz instabilities. Part 2. Energy dissipation rates, evolutions, and statistics. *Journal of Fluid Mechanics*, *941*, A30. https://doi.org/10.1017/jfm.2021.1086

Fritts, D. C., Wang, L., & Werne, J. (2013). Gravity wave–fine structure interactions. Part 1: Influences of fine structure form and orientation on flow evolution and instability. *Journal of the Atmospheric Sciences*, *70*(12), 3710–3734. https://doi.org/10.1175/JAS-D-13-055.1

Geach, C., Hanany, S., Fritts, D. C., Kaifler, B., Kaifler, N., Kjellstrand, C. B., et al. (2020). Gravity wave breaking and vortex ring formation observed by PMC Turbo. *Journal of Geophysical Research: Atmospheres*, *125*(23), e2020JD033038. https://doi.org/10.1029/2020JD033038

Geach, C. P. (2020). *Gravitational and gravity waves: The EBEX and PMC turbo balloon experiments*. Doctoral dissertation. University of Minnesota.

Hecht, J. H., Fritts, D. C., Gelinas, L. J., Rudy, R. J., Walterscheid, R. L., & Liu, A. Z. (2021). Kelvin-Helmholtz billow interactions and instabilities in the mesosphere over the Andes lidar observatory: 1. Observations. *Journal of Geophysical Research: Atmospheres*, *126*(1), e2020JD033414. https://doi.org/10.1029/2020JD033414

Hecht, J. H., Liu, A. Z., Walterscheid, R. L., & Rudy, R. J. (2005). Maui Mesosphere and Lower Thermosphere (Maui MALT) observations of the evolution of Kelvin-Helmholtz billows formed near 86 km altitude. *Journal of Geophysical Research*, *110*, D09S10. https://doi.org/10.1029/2003JD003908

Hecht, J. H., Wan, K., Gelinas, L. J., Fritts, D. C., Walterscheid, R. L., Franke, S. J., et al. (2014). The lifecycle of instability features measured from the Andes lidar observatory over Cerro Pachon on March 24, 2012. *Journal of Geophysical Research: Atmospheres*, *119*, 8872–8898. https://doi.org/10.1002/2014JD021726

Jeong, J., & Hussain, F. (1995). On the identification of a vortex. *Journal of Fluid Mechanics*, *285*, 69–94. https://doi.org/10.1017/S0022112095000462

Kaifler, B., Rempel, D., Roßi, P., Büdenbender, C., Kaifler, N., & Baturkin, V. (2020). A technical description of the Balloon Lidar Experiment (BOLIDE). *Atmospheric Measurement Techniques*, *13*(10), 5681–5695. https://doi.org/10.5194/amt-13-5681-2020

Kaifler, N., Kaifler, B., Rapp, M., & Fritts, D. C. (2022a). The polar mesospheric cloud dataset of the Balloon Lidar Experiment BOLIDE. *Submitted to Earth System Science Data and Atmospheric Chemistry and Physics*.

Kaifler, N., Kaifler, B., Rapp, M., & Fritts, D. C. (2022b). Signatures of gravity wave-induced instabilities in balloon lidar soundings of polar mesospheric clouds. *Submitted to Earth System Science Data and Atmospheric Chemistry and Physics*.

Kelvin, S. W. T. L. (1880). Vibrations of a columnar vortex. *Proceedings of the Royal Society Edinburgh. The London, Edinburgh and Dublin Philosophical Magazine and Journal of Science*, *10*(1880), 443–456.

Kjellstrand, C. B. (2021). *The PMC turbo experiment: Design, development, and results*. Doctoral dissertation. Columbia University.

Kjellstrand, C. B., Jones, G., Geach, C., Williams, B. P., Fritts, D. C., Miller, A., et al. (2020). The PMC Turbo balloon mission to measure gravity waves and turbulence in Polar Mesospheric Clouds: Camera, telemetry, and software performance. *Earth and Space Science*, *7*(8), e2020EA001238. https://doi.org/10.1029/2020EA001238

Klaassen, G. P., & Peltier, W. R. (1985). The onset of turbulence in finite-amplitude Kelvin-Helmholtz billows. *Journal of Fluid Mechanics*, *155*, 1–35. https://doi.org/10.1017/S0022112085001690

Klaassen, G. P., & Peltier, W. R. (1990). Secondary instability and transition in finite amplitude Kelvin-Helmholtz billows. In *Stratified flows* (pp. 35–44). ASCE.

Klaassen, G. P., & Peltier, W. R. (1991). The influence of stratification on secondary instability in free shear layers. *Journal of Fluid Mechanics*, *227*, 71–106. https://doi.org/10.1017/S0022112091000046

Ludlam, F. H. (1967). Characteristics of billow clouds and their relation to clear air turbulence. *Quarterly Journal of the Royal Meteorological Society*, *93*, 419–435. https://doi.org/10.1002/qj.49709339803

Mashayek, A., & Peltier, W. R. (2012a). The 'zoo'of secondary instabilities precursory to stratified shear flow transition. Part 1. Shear aligned convection, pairing, and braid instabilities. *Journal of Fluid Mechanics*, *708*, 5–44. https://doi.org/10.1017/jfm.2012.304

Mashayek, A., & Peltier, W. R. (2012b). The 'zoo'of secondary instabilities precursory to stratified shear flow transition. Part 2. The influence of stratification. *Journal of Fluid Mechanics*, *708*, 45–70. https://doi.org/10.1017/jfm.2012.294

Palmer, T. L., Fritts, D. C., & Andreassen, O. (1996). Evolution and breakdown of Kelvin-Helmholtz billows in stratified compressible flows. Part II: Instability structure, evolution, and energetics. *Journal of the Atmospheric Sciences*, *53*, 3192–3212. https://doi.org/10.1175/1520-0469(1996)053<3192:EABOKB>2.0.CO;2

Palmer, T. L., Fritts, D. C., Andreassen, Ø., & Lie, I. (1994). Three-dimensional evolution of Kelvin-Helmholtz billows in stratified compressible flow. *Geophysical Research Letters*, *21*, 2287–2290. https://doi.org/10.1029/94GL01714

Patnaik, P. C., Sherman, F. S., & Corcos, G. M. (1976). A numerical simulation of Kelvin-Helmholtz waves of finite amplitude. *Journal of Fluid Mechanics*, *73*(2), 215–240. https://doi.org/10.1017/S0022112076001353

Rosenberg, N. W., & Dewan, E. M. (1975). *Stratospheric turbulence and vertical effective diffusion coefficients. Environmental Research Paper 535*. Air Force Cambridge Res. Labs.

Sato, T., & Woodman, R. F. (1982). Fine altitude resolution observations of stratospheric turbulent layers by the Arecibo 430 MHz radar. *Journal of the Atmospheric Sciences*, *39*, 2546–2552. https://doi.org/10.1175/1520-0469(1982)039<2546:FAROOS>2.0.CO;2

Schowalter, D. G., Van Atta, C. W., & Lasheras, J. C. (1994). A study of streamwise vortex structure in a stratified shear flow. *Journal of Fluid Mechanics*, *281*, 247–291. https://doi.org/10.1017/S0022112094003101

Scorer, R. S. (1969). Billow mechanics. *Radio Science*, *4*, 1299–1307. https://doi.org/10.1029/RS004i012p01299

Scorer, R. S., & Wilson, S. D. R. (1963). Secondary instability in steady gravity waves. *Quarterly Journal of the Royal Meteorological Society*, *89*(382), 532–539. https://doi.org/10.1002/qj.49708938208

Thorpe, S. (1971). Experiments on the instability of stratified shear flows: Miscible fluids. *Journal of Fluid Mechanics*, *46*(2), 299–319. https://doi.org/10.1017/S0022112071000557

Thorpe, S. A. (1973a). Experiments on instability and turbulence in a stratified shear flow. *Journal of Fluid Mechanics*, *61*(4), 731–751. https://doi.org/10.1017/S0022112073000911

Thorpe, S. A. (1973b). Turbulence in stably stratified fluids: A review of laboratory experiments. *Boundary Layer Meteorology*, *5*(1–2), 95–119. https://doi.org/10.1007/BF02188314

Thorpe, S. A. (1985). Laboratory observations of secondary structures in Kelvin-Helmholtz billows and consequences for ocean mixing. *Geophysical & Astrophysical Fluid Dynamics*, *34*, 175–199. https://doi.org/10.1080/03091928508245442

Thorpe, S. A. (1987). Transitional phenomena and the development of turbulence in stratified fluids: A review. *Journal of Geophysical Research*, *92*(C5), 5231–5248. https://doi.org/10.1029/JC092iC05p05231

Thorpe, S. A. (2002). The axial coherence of Kelvin–Helmholtz billows. *Quarterly Journal of the Royal Meteorological Society*, *128*(583), 1529–1542. https://doi.org/10.1002/qj.200212858307

Werne, J., & Fritts, D. C. (1999). Stratified shear turbulence: Evolution and statistics. *Geophysical Research Letters*, *26*, 439–442. https://doi.org/10.1029/1999GL900022

Witt, G. (1962). Height, structure and displacements of noctilucent clouds. *Tellus*, *14*(1), 1–18. https://doi.org/10.3402/tellusa.v14i1.9524

Woodman, R. F., & Rastogi, P. K. (1984). Evaluation of effective eddy diffusive coefficients using radar observations of turbulence in the stratosphere. *Geophysical Research Letters*, *11*, 243–246. https://doi.org/10.1029/GL011i003p00243

Woods, J. D. (1968). Wave-induced shear instability in the summer thermocline. *Journal of Fluid Mechanics*, *32*(4), 791–800. https://doi.org/10.1017/S0022112068001035

Woods, J. D., & Wiley, R. L. (1972). Billow turbulence and ocean microstructure. *Deep Sea Research*, *19*, 87–121. https://doi.org/10.1016/0011-7471(72)90043-5